Evolution of complex magnetic phases and metal-insulator transition through Nb substitution in La$_{0.5}$Sr$_{0.5}$Co$_{1-x}$Nb$_x$O$_3$

Rishabh Shukla and R. S. Dhaka [*]

Department of Physics, Indian Institute of Technology Delhi, Hauz Khas, New Delhi-110016, India

We report the evolution of structural, magnetic, transport, and electronic properties of bulk polycrystalline La$_{0.5}$Sr$_{0.5}$Co$_{1-x}$Nb$_x$O$_3$ ($x = 0.025$–0.25) samples. The Rietveld refinement of the x-ray diffraction patterns with $R\bar{3}c$ space group reveals that the lattice parameters and rhombohedral distortion monotonously increase with the Nb^{5+}($4d^0$) substitution (x). The magnetic susceptibility exhibits a decrease in the magnetic ordering temperature and net magnetization with x, which manifests that the Nb substitution dilutes the ferromagnetic (FM) double-exchange interaction and enhances the antiferromagnetic (AFM) superexchange interaction. Interestingly, for the $x > 0.1$ samples the FM order is completely suppressed and the emergence of a glassy state is clearly evident. Moreover, the decrease in the coercivity (H_C) and remanence (M_r) with x in the magnetic isotherms measured at 5 K further confirms the dominance of AFM interactions and reduction of FM volume fraction for the $x > 0.1$ samples. More interestingly, we observe resistivity minima for the $x = 0.025$ and 0.05 samples, which are analyzed using the quantum corrections in the conductivity, and found that the weak localization effect dominates over the renormalized electron-electron interactions in the three-dimensional (3D) limit. Further, a semiconducting resistivity behavior is obtained for $x > 0.05$, which follows the Arrhenius law at high temperatures ($\sim$160–320 K), and the 3D variable range hopping prevails in the low-temperature region ($<$160 K). The core-level photoemission spectra confirm the valence state of constituent elements and the absence of Co^{2+} is discernible.

I. INTRODUCTION

The exotic physical properties of LaCoO$_3$ are predominantly associated with the spin-state transition of Co^{3+} [1–7], where it exhibits a nonmagnetic charge transfer type insulating ground state below $\sim$100 K and an insulator-to-metal transition near about 500 K [3,4]. The ground state of LaCoO$_3$ is associated with the Co^{3+} low-spin (LS) state ($t_{2g}^6 e_g^0$), which evolves to a paramagnetic state (near 100 K) due to the emergence of high-spin (HS; $t_{2g}^4 e_g^2$) and/or intermediate-spin (IS; $t_{2g}^5 e_g^1$) states. The transition around 100 K was believed to be from LS to HS state [8–10]; however, this explanation was amended with the inclusion of the IS state, which was introduced in Ref. [11] by LDA$+U$ band structure calculations. At the same time, the evolution of the spin-state transition with external perturbation still remains enigmatic after several efforts, where a combination of the LS/IS scenario was supported in the explanation of insulator-to-metal transition near 500 K [4,11], which contradicts with the description given using the LS/HS combination [1,7]. Interestingly, the presence of Jahn-Teller distortion in LaCoO$_3$ strengthens the presence of IS state [12–15]. Moreover, the IS state of Co^{3+} is energetically near to the LS state (difference of $\sim$10 meV) and exists at lower energy as compared to the HS state, while in Co^{4+} the HS state has a lower energy ($\sim$1 eV) with respect to the LS state [2,5,11]. This energy difference (ΔE) between the spin states of Co ions can be controlled by the volume of the governing CoO$_6$ octahedron via various external parameters like temperature and mechanical pressure [14], magnetic field [15], and chemical pressure [16–18]. This great tunability of the physical properties of cobaltites make them fascinating for practical applications, like catalysis [19], solid oxide fuel cells [20], sensors [21], batteries [22,23], etc.

Intriguingly, the substitution of divalent cations (like Ca, Sr, Ba) at La^{3+} site results in the emergence of tetravalent Co^{4+} ions, and a chemical pressure effect increases the lattice volume owing to the larger ionic radii of divalent cations, and a dramatic modification in the magnetic, and transport properties are observed [16,17,24,25]. According to Imada *et al.*, the La$_{1-x}$Sr$_x$CoO$_3$ is a distinct filling-control system, where holes are solely responsible for the metallic conduction and ferromagnetism [25]. Also, the substitution of larger size Sr^{2+} (1.44 Å) as compared to La^{3+} (1.36 Å) enhances the crystal symmetry and unit-cell volume, which are believed to stabilize the IS state of Co^{3+} ions and do not change the structure up to $x = 0.55$ [16,17,26]. Moreover, the magnetic phase diagram of La$_{1-x}$Sr$_x$CoO$_3$ manifests a spin-glass state in $0.05 < x \leqslant 0.18$ and a ferromagnetic cluster glass for $0.18 \leqslant x \leqslant 0.50$ due to the dominance of double-exchange ferromagnetic (FM) interaction (Co^{3+}-O^{2-}-Co^{4+}) over the superexchange (Co^{4+}-O^{2-}-Co^{4+})/(Co^{3+}-O^{2-}-Co^{3+}) interactions [17,27–31]. Also, an insulator-to-metal transition is induced for $x \geqslant 0.18$ and further evolves to a complete metallic state for $x \geqslant 0.30$ [17,27], and the magnetoelectronic phase separation is reported up to $x = 0.5$ where FM

---
[*]rsdhaka@physics.iitd.ac.in

metallic clusters are embedded in the AFM insulating matrix [18,32]. More interestingly, the substitution of Nb^{5+} $(4d^0)$ in $LaCo_{1-x}Nb_xO_3$ converts Co^{3+} into Co^{2+} and induces structural transition owing to the larger ionic radius of Nb^{5+} (0.64 Å) and Co^{2+} (0.75 Å) as compared to Co^{3+} (0.55 Å) [6,24]. The substitution of Nb^{5+} induces the enhancement in the unit-cell volume and stabilizes the HS state of Co^{3+} and Co^{2+} ions and drives the system towards a more insulating nature [6]. Also, the perovskite cobaltites exhibit a strong coupling between the spin, charge, and lattice, where the correlation between charge carriers and localized spins plays a crucial role [33,34], and can be tuned by cation substitution [35,36]. Overall, it is convincing that the substitution of Sr at the La site and/or Nb at the Co site demonstrate interesting changes in the physical properties of $LaCoO_3$ (diamagnetic insulator) [37,38]. However, to the best of our knowledge, a study to examine the effect of Nb substitution at the Co site in $La_{0.5}Sr_{0.5}CoO_3$ (ferromagnetic metal) has not been explored.

Therefore, in this paper, we investigate the evolution of structural, magnetic, transport, and electronic properties of bulk $La_{0.5}Sr_{0.5}Co_{1-x}Nb_xO_3$ ($x = 0.025–0.25$) samples. The Rietveld refinement of x-ray diffraction (XRD) patterns reveals the monotonous increase of unit-cell parameters and rhombohedral distortion with x. The temperature-dependent susceptibility manifests the dilution of the magnetic order with x due to nonmagnetic $Nb^{5+}(4d^0)$, which dominates for $x > 0.1$, and the appearance of a glassy state is evident. Moreover, the isothermal MH loops measured at 5 K manifest that coercivity (H_C) and remanence (M_r) decrease for $x > 0.1$ due to the dominance of antiferromagnetic (AFM) interactions and reduction of FM volume fractions. More interestingly, we observe resistivity minima for the $x = 0.025$ and 0.05 samples, which are analyzed using the quantum corrections in the conductivity, and find that the weak localization effect dominates over the renormalized electron-electron interactions in the three-dimensional (3D) limit. Moreover, a semiconducting behavior for the $x \geqslant 0.075$ is analyzed with the Arrhenius model at high temperatures (~160–320 K) and 3D variable range hopping conduction prevails in the low-temperature region (<160 K). Furthermore, the oxidation state of elements in $La_{0.5}Sr_{0.5}Co_{1-x}Nb_xO_3$ ($x = 0.1, 0.15, 0.25$) is studied using core-level photoemission spectroscopy.

II. EXPERIMENT

The polycrystalline samples of $La_{0.5}Sr_{0.5}Co_{1-x}Nb_xO_3$ ($x = 0.025–0.25$) are synthesized through the conventional solid-state route using stoichiometric initial ratio of as purchased powders (purity >99.95%) of $SrCoO_3$, Co_3O_4, and Nb_2O_5 and dried La_2O_3 (900 °C for 6 h). All the initial powders are grinded for 6–8 h using the agate mortar pestle and then obtained material is heated at 1000 °C for 48 h to ensure homogeneous mixing. After the first heating, obtained mixture is reground for 4–6 h and cold pressed into pellets for the final heating of 1200–1400 °C for 36 h, which ensures the formation of a pure-phase compound [6,13]. The structural characterizations are performed at room temperature with the Panalytical X'pert Pro diffractometer using the Cu-K_α radiation ($\lambda = 1.5406$ Å). The magnetic measurements are performed using DynaCool Magnetic Property

Measurement System (MPMS) from Quantum Design, USA. The temperature-dependent resistivity measurements were performed at the Physical Property Measurement System (PPMS) from Cryogenic Limited, UK, and the PPMS from Quantum Design, USA. The core-level x-ray photoemission spectra are recorded at room temperature using the AXIS Supra from the company Kratos Analytical limited, using a monochromatic Al-K_α (1486.6 eV) source having an overall energy resolution of ~0.5 eV. We use the charge neutralizer during the measurement due to the insulating nature of the samples. The core-level spectra are deconvoluted and fitted with the Voigt-peak shapes using IGORPRO software after subtracting the Tougaard inelastic background.

III. RESULTS AND DISCUSSION

First, we perform the Rietveld refinement of measured XRD patterns of the $La_{0.5}Sr_{0.5}Co_{1-x}Nb_xO_3$, as presented in Figs. 1(a)–1(h) for the $x = 0.025–0.25$ samples, respectively, which confirm the single phase and rhombohedral space group ($R\bar{3}c$) in hexagonal setting ($a = b$, and $\gamma = 120^o$). The Rietveld refined lattice parameters are summarized in Table I of [39] including the unit-cell parameters determined for an equivalent rhombohedral cell (a_r and α_r) in the rhombohedral setting of the $R\bar{3}c$ space group. Interestingly, the rhombohedral and hexagonal lattices are correlated via the symmetry transformation and, therefore, the Rietveld refinement using rhombohedral space group ($R\bar{3}c$) in a hexagonal setting will also result in the values of rhombohedral unit-cell parameters, i.e., cell length (a_r) and distortion angle (α_r). Further, the x dependence of the unit-cell parameters is plotted in Fig. 1(i): $a = b$ (open blue circles) and a_r (solid blue circles) on the left axis, and c (open red triangles) on the right axis. Here, we observe a monotonous enhancement in the values of these parameters with increasing the x. Moreover, we find an enhancement in the rhombohedral angle (α_r) and unit-cell volume (V) with the x, as shown on the left (open blue inverted triangles) and right (open red pentagons) axes of Fig. 1(j), respectively. This systematic monotonous enhancement in structural parameters with x is accredited to the large ionic radii of Nb^{5+} (0.64 Å) as compared to the Co^{3+} (0.545 Å in LS and 0.61 Å in HS) and Co^{4+} (0.53 Å in HS) ions [24]. Further, the enhancement in α_r manifests that the cationic substitution results in a higher degree of distortion of (Co/Nb)O_6 octahedra and therefore participates in the evolution of the spin states of Co ions with Nb substitution (discussed later) [40]. It has been reported that the substitution of Sr^{2+} at the La site in $LaCoO_3$ suppresses the rhombohedral distortion (α_r) and cubic crystal symmetry ($Pm\bar{3}m$) dominates for $x \geqslant 0.55$ [17,26], whereas the substitution of Nb^{5+} at Co site drives the rhombohedral crystal symmetry from orthorhombic and then to monoclinic [6]. Intriguingly, in the present case, the observation of an enhancement in the α_r with x demonstrates a dominance of Nb^{5+} ions on the structural parameters. Moreover, the observation of sharper diffraction peaks with much higher intensity (30–60 K) indicates the absence of any microscopic inhomogeneities in these samples [41].

As discussed in the Introduction, it is interesting to note here that the phenomenon of double-exchange interaction in the Co^{3+}(IS)-O-Co^{4+}(LS) path is found to be responsible
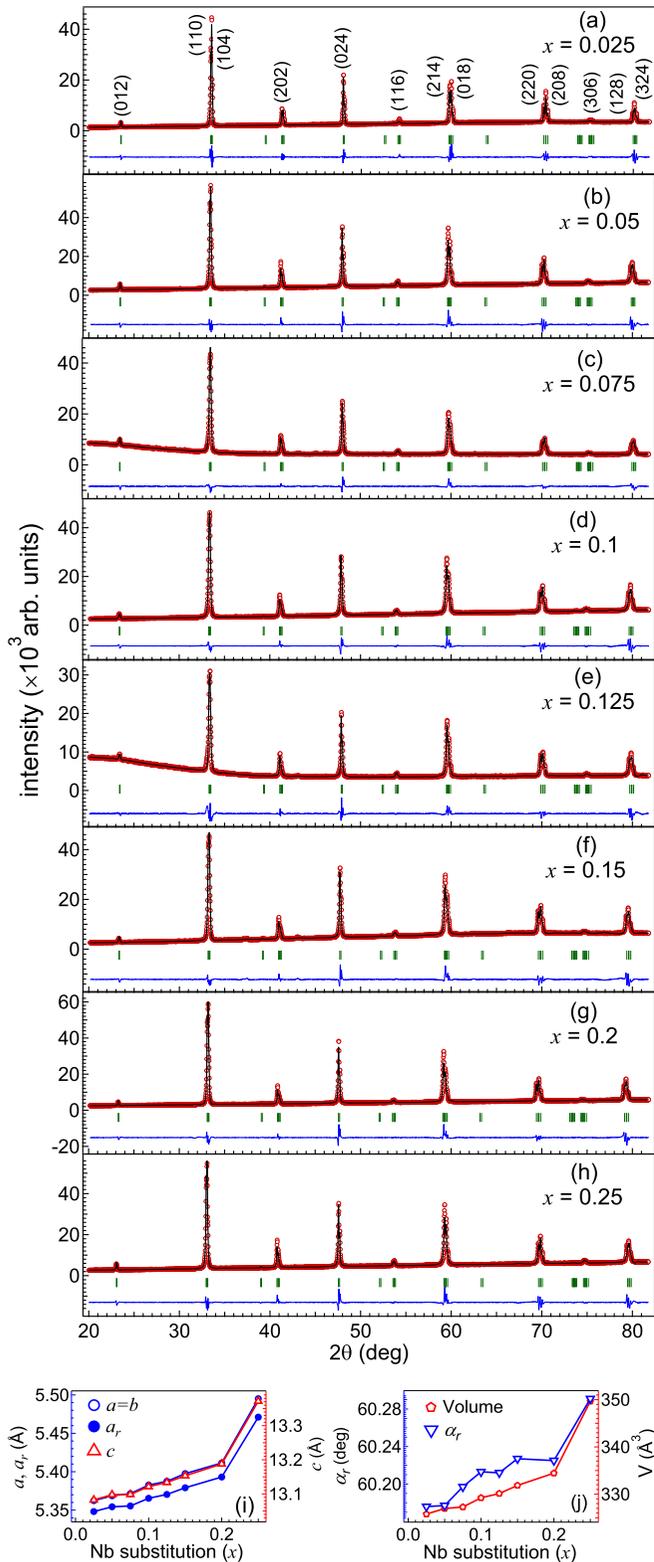
FIG. 1. (a)–(h) The Rietveld refined XRD patterns of La$_{0.5}$Sr$_{0.5}$Co$_{1-x}$Nb$_x$O$_3$ (x = 0.025–0.25) samples, where open red circles, solid black, and blue lines represent the experimental, refined, and difference between experimental and refined patterns, while green vertical markers manifest the Bragg positions corresponding to the $R\bar{3}c$ space group. (i), (j) The Rietveld refined unit-cell parameters plotted as a function of x.

for the itinerant FM in La$_{0.5}$Sr$_{0.5}$CoO$_3$, which is achieved due to the spin pumping owing to the Sr^{2+} substitution that converts Co^{3+} ions into the Co^{4+} ions and stabilizes the IS state of Co^{3+} [16,17,27]. More interestingly, in the present case, the nonmagnetic Nb^{5+} ($4d^0$) substitution acts as a magnetic dilution in the FM state of La$_{0.5}$Sr$_{0.5}$CoO$_3$, and that suppresses the long-range FM ordering as Nb^{5+} converts Co^{4+} back to Co^{3+} and hence reduces the double-exchange mechanism. Also, in this case, the increased concentration of Co^{3+} enhances the dominance of AFM superexchange interaction through the Co^{3+}-O-Co^{3+} path [42,43]. Therefore, in order to understand the expected complex magnetic behavior with Nb substitution in La$_{0.5}$Sr$_{0.5}$Co$_{1-x}$Nb$_x$O$_3$, we measure the temperature-dependent zero-field cooled (ZFC) and field-cooled (FC) magnetization at applied magnetic fields of 100 Oe (for the x = 0.025–0.25) and 1000 Oe (for the x = 0.025–0.15), as shown in Figs. 2(a)–2(f). Interestingly, we find a complex magnetic ordering below the transition temperature, as shown in Figs. 2(a)–2(d), for x = 0.025–0.1 samples, respectively, and also highlighted in Figs. 1(a) and 1(b) of [39] by plotting the first-order derivative of the dc susceptibility. The sharp minima in Fig. 1(a) of [39] are clearly visible at 207 and 204 K for the x = 0.025 and 0.05 samples, respectively, measured at 100 Oe. Similarly, the minima are found to be at 135 and 130 K for the x = 0.075 and 0.1 samples, respectively, as shown in Fig. 1(b) of [39].

It reveals that the magnetic ordering temperature is sensitive to the measuring field [44], and we find that a small substitution of Nb^{5+} ($4d^0$) significantly suppresses the magnetic ordering temperature (T_{MO}) from 250–253 K for the x = 0 sample [41,45] to 205 ± 2 K for the x = 0.025 sample, which may define the onset of magnetic dilution. Also, in Fig. 2(a), the maximum FC magnetic susceptibility decreases from ∼20 emu mole^{-1} Oe^{-1} (x = 0) [44,45] to 15 emu mole^{-1} Oe^{-1} (x = 0.025), and from ∼5.5 emu mole^{-1} Oe^{-1} (x = 0) [46,47] to 4.8 emu mole^{-1} Oe^{-1} (x = 0.025) when the measurements are done at 100 and 1000 Oe, respectively. This type of complex magnetic ordering remains enigmatic in literature; for example, it is believed to be FM cluster glass [17,27] and/or FM to paramagnetic transition [28,48]. Furthermore, in Figs. 2(a) and 2(b), the FC magnetization increases monotonously up to the lowest measured temperature (2 K), whereas the ZFC magnetization shows a cusp with broad peaks at around 183 and 176 K (100 Oe) and 108 and 88 K (1000 Oe) for the x = 0.025 and 0.05 samples, respectively. It has been reported that the cusp in the ZFC magnetization can be associated with the anisotropy in the FM clusters available in the AFM matrix, and that is associated with the intracluster interaction and intercluster anisotropy in the matrix [49]. Interestingly, a large bifurcation between the ZFC and FC magnetizations further confirms the higher anisotropy in these samples [17]. However, we find that this anisotropy decreases with the substitution of Nb^{5+} ions and applied magnetic field, which plays a crucial role in the suppression of the intracluster FM interactions.

More importantly, we find a drastic change in the behavior of ZFC and FC magnetization curves for the x = 0.075 and 0.1 samples, which exhibit a decreasing trend below a cusp and then remain constant to 2 K, as shown in Figs. 2(c) and 2(d).
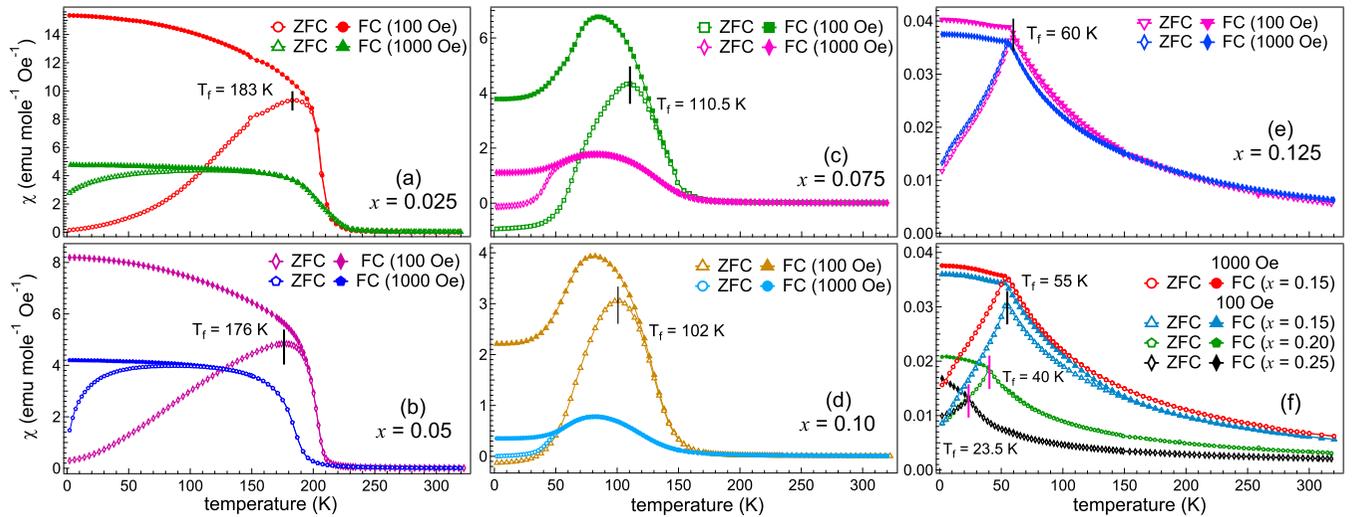
FIG. 2. A comparison of the temperature-dependent zero-field-cooled (ZFC) and field-cooled (FC) dc magnetic susceptibility data recorded at 100 and 1000 Oe applied magnetic field for the (a) $x = 0.025$, (b) $x = 0.05$, (c) $x = 0.075$, (d) $x = 0.1$, (e) $x = 0.125$, (f) $x = 0.15$, $x = 0.2$ (100 Oe), and $x = 0.25$ (100 Oe) samples.

Here, the values of FC magnetic susceptibility at the peak are found to be around 6.8 emu mole^{-1} Oe^{-1} (100 Oe) and 1.8 emu mole^{-1} Oe^{-1} (1000 Oe) for the $x = 0.075$ sample, and 3.9 emu mole^{-1} Oe^{-1} (100 Oe) and 0.8 emu mole^{-1} Oe^{-1} (1000 Oe) for the $x = 0.1$ sample. These values decrease below ≈ 83 K and almost saturate to around 3.8 emu mole^{-1} Oe^{-1} (100 Oe), 1.1 emu mole^{-1} Oe^{-1} (1000 Oe), and 2.2 emu mole^{-1} Oe^{-1} (100 Oe), 0.35 emu mole^{-1} Oe^{-1} (1000 Oe) at the lowest measured temperature (2 K) for the $x = 0.075$ and 0.1 samples, respectively. The decreasing behavior of FC magnetic susceptibility is usually observed in the samples with an antiferromagnetic ordering [50] and/or samples with a higher volume fraction of the AFM interactions as compared to the FM interactions [51,52]. The magnetization values are found to be further decreasing with x, which is consistent with the fact that more Nb^{5+} ($4d^0$) concentration acts like a magnetic dilution. Further, the difference between FC and ZFC magnetizations (ΔM, thermomagnetic irreversibility) at the lowest temperature is correlated with the presence of FM and/or AFM volume fraction in the sample. A decrease in the value of ΔM with x is observed, i.e., 472 emu mole^{-1} (100 Oe), 1240 emu mole^{-1} (1000 Oe) for the $x = 0.075$, and 234 emu mole^{-1} (100 Oe), 350 emu mole^{-1} (1000 Oe) for the $x = 0.1$ sample [see the left axis, solid red circles (100 Oe) and solid black rhombus (1000 Oe), of Fig. 3(d)]. This suggests that we are restricted to collect the magnetization from the smaller volume fraction of FM and higher fraction of AFM phase with increasing x [51]. The ZFC magnetic susceptibility values are found to be negative at 2 K when measured at 100 Oe magnetic field, which become less negative when measured at 1000 Oe for the $x = 0.075$ and 0.1 samples [see Figs. 2(c) and 2(d)]. Here, the observed negative magnetization in ZFC is possibly due to the residual negative field of the superconducting magnet of the MPMS [53]. Also, a large magnetic anisotropy due to the strong competitive AFM and FM interactions might be responsible for the field- and temperature-induced magnetization reversal behavior [54,55], which is consistent with the observed

variation in ΔM with the applied magnetic field. Interestingly, we observe a further decrease in the T_{MO} to 135 K ($x = 0.075$) and 130 K ($x = 0.1$) measured at 100 Oe [see also Fig. 1(b) of [39]], and an increase in the broadening of the transition temperature region with x can be attributed to the enhanced magnetic disorder in the material and dilution of the FM double-exchange interaction [56–58]. Moreover, in Figs. 2(c) and 2(d), the cusp and peak in the FC and ZFC magnetizations at 100 Oe are observed at different temperatures like 83.5 and 110.5 K ($x = 0.075$) and 82 and 102 K ($x = 0.1$), respectively. The corresponding values at 1000 Oe are found to be 82 and 84 K ($x = 0.075$), and 80 and 81.5 K ($x = 0.1$), respectively. The peak and cusp in the FC curves appear at a lower temperature as compared to the ZFC, which is due to the difference in the measurement protocols as the FC measures the higher FM volume fraction compared to the ZFC protocol [51]. Therefore, confirmation of the decreased FM volume fraction in higher x samples is obtained from a smaller difference in the cusp and peak value of FC and ZFC magnetizations, i.e., $\Delta T_f = 27$ K (100 Oe), 2 K (1000 Oe) for the $x = 0.075$ sample, and 20 K (100 Oe), 1.5 K (1000 Oe) for the $x = 0.1$ sample. Furthermore, the ZFC and FC susceptibilities remain constant from ~ 35 K (100 Oe) and 28 K (1000 Oe) to the lowest measured temperature for both the FC and ZFC protocols [see Figs. 2(c) and 2(d)], and this is expected to be a state of magnetic glass where the competitive FM and AFM magnetic clusters are frozen arbitrarily in the sample at low temperatures [51].

Intriguingly, for the $x = 0.125$–0.25 samples we find a substantial change in the magnetic behavior, as shown in Figs. 2(e) and 2(f), respectively. For example, the FM ordering is suppressed due to reduction in the concentration of Co^{4+} ions and the evolution of AFM interactions due to an enhancement in Co^{3+}, which may result in the evolution of a glassy state [59,60] for the $x \geqslant 0.125$ samples. The magnetic susceptibility value at 2 K dropped abruptly to 0.04 emu mole^{-1} Oe^{-1} for the $x = 0.125$ and 0.15 samples, which indicates that the magnetic order is very much
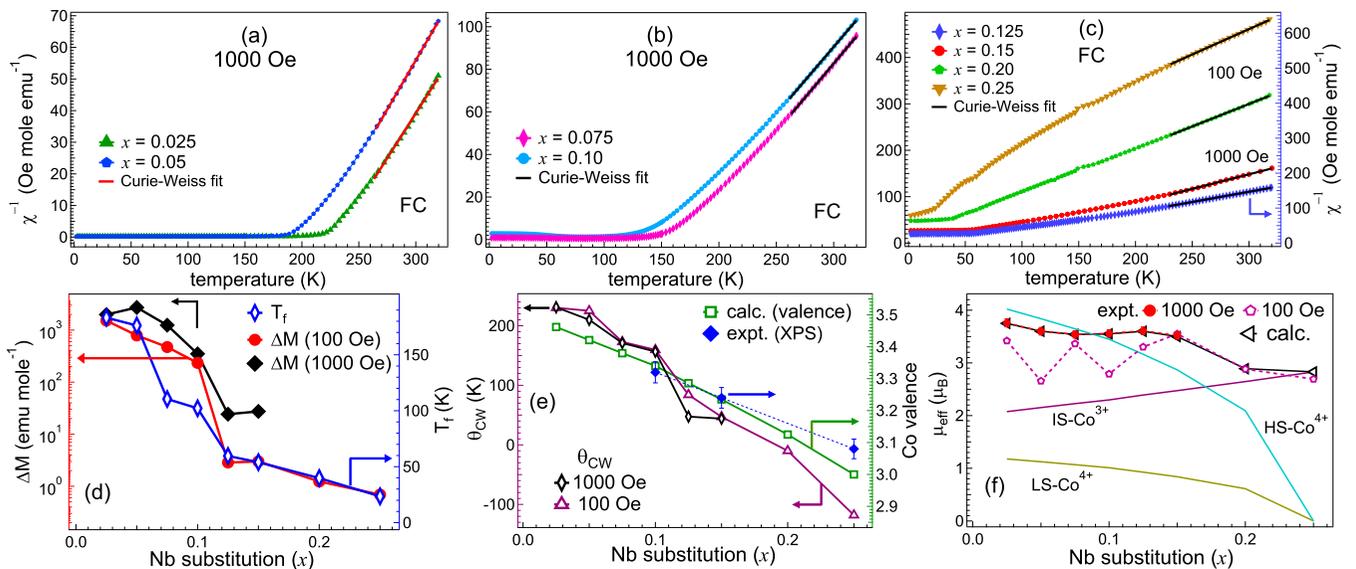
FIG. 3. A linear fit (solid red and black lines) of the inverse susceptibility data (recorded at 100 and/or 1000 Oe) manifests the Curie-Weiss law in the paramagnetic region of (a) 260–320 K for the $x = 0.025$ and 0.05 samples, (b) 260–320 K for the $x = 0.075$ and 0.1 samples, (c) 230–320 K for the $x = 0.125$–0.25 samples. (d) The thermomagnetic irreversibility ΔM for 100 Oe (solid red circles) and 1000 Oe (solid black rhombus) on a semilogarithmic left axis, and peak/freezing (T_f) temperature from the ZFC magnetization (open blue rhombus) on right axis as a function of x, and (e) the Curie-Weiss temperature θ_{CW} for 100 Oe (open magenta triangles) and 1000 Oe (open black rhombus) along with the average cobalt valence n [open green rectangles (calculated) and solid blue rhombus (experimentally obtained using XPS)], and (f) a comparison of experimentally determined values of effective magnetic moments for susceptibility data recorded at 100 and 1000 Oe magnetic fields and theoretically calculated values considering different possible spin states of the Co ions.

sensitive to the percolation limit in the $La_{0.5}Sr_{0.5}Co_{1-x}Nb_xO_3$ samples. Moreover, we can see that all samples in the $0.125 \leqslant x \leqslant 0.25$ range manifest analogous behavior of FC and ZFC magnetization curves with temperature [see Figs. 2(e) and 2(f)], where both the FC and ZFC magnetizations increase monotonously with lowering the temperature, and after a peak/cusp in ZFC (known as the freezing temperature T_f), the FC magnetization further increases at a lower rate while the ZFC magnetization starts decreasing up to the lowest measured temperature (2 K). Additionally, we observe that the freezing temperature T_f (peak/cusp in ZFC) decreases with x [see right axis (open blue rhombus) of Fig. 3(d)], such that it has the value of 58 ± 2 K ($x = 0.125$), ≈ 55 K ($x = 0.15$), 40 K ($x = 0.2$), and 23.5 K ($x = 0.25$). Also, the value of ΔM measured at 100 Oe decreases from 3 emu mole^{-1} for the $x = 0.125$ to 0.7 emu mole^{-1} for the $x = 0.25$ sample, as shown on the left axis (solid red circles) of Fig. 3(d), which further suggests a minimal volume fraction of the FM magnetic phase in these samples as discussed above. Therefore, we can conclude that the substitution of Nb^{5+} ($4d^0$) plays a crucial role in the dilution of the FM order and inducing a magnetic glassy state at low temperatures [59–61].

In order to determine the effective magnetic moment (μ_{eff}), we plot the inverse FC magnetic susceptibility in Figs. 3(a)–3(c) for the $x = 0.025$–0.15 (1000 Oe) and the $x = 0.2$, 0.25 (100 Oe) samples. Moreover, the inverse susceptibility data for the $x = 0.025$–0.15 samples measured at 100 and 1000 Oe are compared in the Figs. 2(a)–2(f) of [39]. We fit the inverse susceptibility data using the Curie-Weiss (CW) equation [$\chi^{-1} = (T - \theta_{CW})/C$], where C is CW constant and θ_{CW} is CW temperature in the paramagnetic region for all the $La_{0.5}Sr_{0.5}Co_{1-x}Nb_xO_3$ samples. The obtained slope in the

CW fit, for the $x = 0.025$–0.15 (1000 Oe) and $x = 0.2$, 0.25 (100 Oe) samples, is used to determine the μ_{eff} and the intercept is utilized to estimate the θ_{CW}, which are summarized in Table II of [39]. Further, we plot the x dependence of μ_{eff} (solid red circles for 1000 Oe and open magenta pentagon for 100 Oe) in Fig. 3(f), which shows a monotonous decrease in the values as a function of x. Additionally, we observe a monotonous decrease in the θ_{CW} values (magenta open triangles, left axis) as well as the calculated average Co valence n (green open rectangles) with x, as shown in Fig. 3(e). The value of n is calculated using the general formula of $La_{0.5}^{3+}Sr_{0.5}^{2+}Co_{1-x}^{n}Nb_x^{5+}O_3^{2-}$, where x is the percentage of Nb substitution. Here, the experimentally obtained values of the Co valence state (solid blue rhombus) from the core-level photoemission spectra of Co $2p$ are also compared (discussed later), which matches well for the $x = 0.1$ and 0.15 samples, while slightly deviates for the $x = 0.25$ sample [see Fig. 3(e)]. Note that, the decreasing trend of these parameters manifests an overall evolution of the AFM interactions over FM interactions and reduction of the magnetic anisotropy with x [62]. Moreover, we calculate the theoretical value of μ_{eff}^{calc} using the equation $\mu_{eff}^{calc} = \sqrt{(1 - p)[\mu_{eff}^{4+}]^2 + p[\mu_{eff}^{3+}]^2}$, where p is the fraction of the Co^{3+} ions, and the μ_{eff}^{4+} and μ_{eff}^{3+} correspond to the 4+ and 3+ valence states of Co, respectively. These theoretically calculated values of μ_{eff}^{calc} considering different spin states of Co^{3+} and Co^{4+} ions. For the $x = 0$ sample, Xu et al. reported that the Co^{3+} ions present in the IS state, whereas the Co^{4+} ions stabilize in a mixture of LS and HS states [63]. Similarly, we calculate the μ_{eff} values considering composition weighted spin states of Co^{3+}/Co^{4+} ions in $La_{0.5}Sr_{0.5}Co_{1-x}Nb_xO_3$, which are plotted in Fig. 3(f) as a function of x. The calculated values of μ_{eff} are found to be in
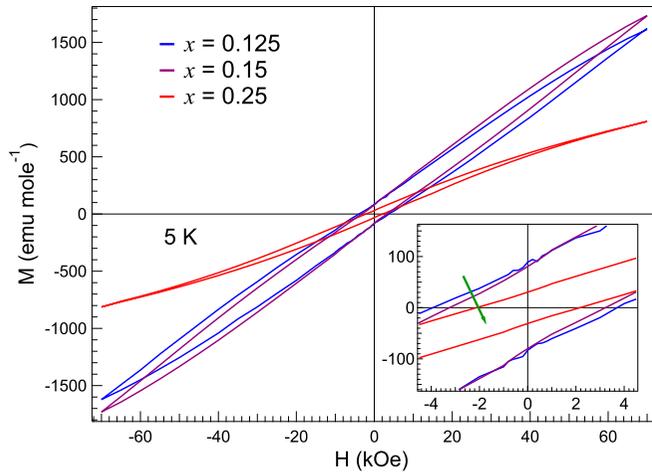
FIG. 4. The isothermal *M-H* loops recorded at 5 K within the applied magnetic field of ±70 kOe for the $x = 0.125, 0.15$, and 0.25 samples; the inset highlights the variation of magnetization near the zero-magnetic field.

good agreement with the experimental $\mu_{\text{eff}}^{\text{expt}}$ values, as shown in Fig. 3(f). All the extracted parameters are summarized in Table II of [39].

Furthermore, to understand the magnetic interaction in the highly competitive FM and AFM regions, we measure the isothermal *MH* loops for the $x = 0.125, 0.15$, and 0.25 samples at 5 K within ±70 kOe applied magnetic field under the ZFC protocol and shown in Fig. 4. Interestingly, a nonsaturating symmetric behavior observed in the magnetization is due to the constant increase of spin reorientation in the field direction. The estimated values of coercivity (H_C) are found to be 3.8, 3.2, and 2.2 kOe, and the remanence (M_r) values are 86, 80, and 31 emu/mole for the $x = 0.125, 0.15$, and 0.25 samples, respectively. We find that the values of H_C and M_r decrease with increasing the x, as highlighted with a green arrow in the inset of Fig. 4, which manifests that the higher Nb^{5+} ($4d^0$) concentration suppresses the volume fraction of the spin-pinning boundaries as well as the nonhomogeneity of the magnetic phase [29]. Moreover, the virgin isothermal curves measured at 5 K deviate from the linear behavior and show an upturn at higher fields (convex nature) [see Fig. 3(a) of [39]], which suggests a metamagnetic nature for the $x = 0.125$ and 0.15 samples. A more closer look indicates two critical magnetic fields at ≈16 (H_{m_1}) and 35 kOe (H_{m_2}) [arrows in Figs. 3(b) and 3(c) of [39]] [64]. These can be associated with competitive AFM and FM interactions at low fields; however, a linear increase of magnetization beyond H_{m_2} suggests that AFM interactions dominate at higher fields [64,65]. However, for the $x = 0.25$ sample, the saturating nature of the *M-H* curve at high magnetic fields (>40 kOe) manifests the field-induced spin reorientation [66].

To investigate the temperature-dependent transport behavior in $La_{0.5}Sr_{0.5}Co_{1-x}Nb_xO_3$, first the ρ-T curves are compared in Fig. 5(a) for the $x = 0.025$ and 0.05 samples. The resistivity varies linearly above $T_{\text{MO}} \sim 250$ K, whereas a gradual change in the slope, i.e., a subtle decrease in the resistivity below T_{MO} can be correlated to the conversion of Co^{3+} ions from HS state to IS state in this temperature range.
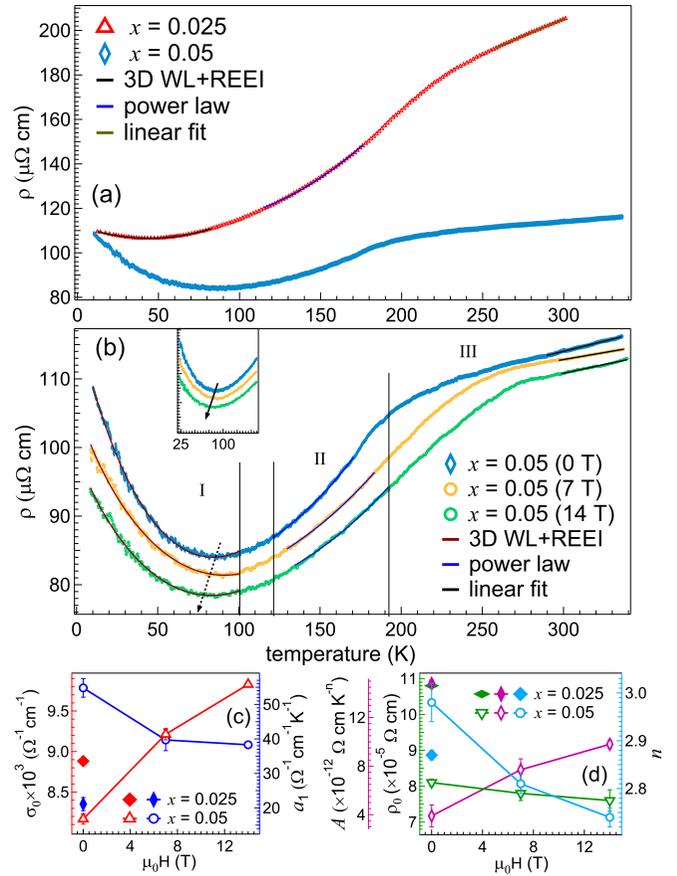
FIG. 5. (a) A comparison of the temperature-dependent resistivity of the $x = 0.025$ and 0.05 samples at zero magnetic field, (b) the variation in resistivity with the applied magnetic field (0, 7, and 14 T) for the $x = 0.05$ sample, experimental and fitted data are shown in the open symbols and solid lines, respectively. The inset in (b) highlights the decrease in the resistivity minimum (T_{min}) with the magnetic field. (c) The variation of the low-temperature (below 100 K) fitting parameters using Eq. (1), σ_0 (left axis) and a_1 (right axis), and (d) the variation in fitting parameters in 120–200 K range using Eq. (3), A (first left axis), ρ_0 (second left axis), and power-law exponent (n) with the magnetic field (for the $x = 0.05$ sample) and for both the $x = 0.025$ and 0.05 samples at the zero-magnetic field.

The changes can be attributed to the reduction in the scattering because of the spin disorder owing to the FM ordering in the sample below T_{MO} [67]. Interestingly, we observe a minimum (T_{min}) near 77 and 83 K for the $x = 0.025$ and 0.05 samples, respectively, as shown in Fig. 5(a). The resistivity increases below T_{min}, which is the signature of metal-to-insulator transition (T_{MI}), and can be associated with the spin-state transition from the IS to the LS state [12]. The metallic nature in the $x = 0.025$ and 0.05 samples can be understood due to the presence of a larger volume fraction of Co^{4+} ions, as in $La_{1-x}Sr_xCoO_3$ for $x \geqslant 0.18$ [17]. Interestingly, a similar resistivity behavior is reported near $T \sim 100$ K in magnetic oxides [68] and is believed to be a disorder-induced effect [34] as well as this temperature scales with the spin-state transition of Co ions from HS to IS [4,6]. Further, at low temperatures, the resistivity starts increasing and that indicates the transition of Co^{3+} ions to the LS state, as reported for $LaCoO_3$ [4,6]. In Fig. 5(b)

we compare the ρ-T behavior of $x = 0.05$ sample measured at 0, 7, and 14 T applied magnetic fields. The applied magnetic field enhances the exchange interaction strength and the observed negative magnetoresistance behavior below ≈ 100 K can be associated with the enhanced density of states near the Fermi level [69]. Intriguingly, in the quantum transport regime at low temperatures, the phenomenon of weak localization (WL) or weak antilocalization (WAL) correction in the conductivity arises due to the interference of the electron waves traveling back and forth in the material and is termed as the quantum corrections in the conductivity (QCC) [34]. The negative magnetoresistance in the $x = 0.05$ sample manifests the dominance of WL as the field suppresses the magnetic disorder and hence the resistivity [34]. Also, the interference of the two different electron waves gives rise to the renormalized electron-electron interaction (REEI) [34]. Therefore, a least-square minimization method is used to fit the experimental data by considering the contributions of WL and REEI in both three-dimensional (3D) and two-dimensional (2D) limits.

The ρ-T behavior can be approximated by the following Eqs. (1) and (2) for the 3D and 2D limits of WL and REEI effects, respectively [34,70]:

$$\rho(T) = \frac{1}{(\sigma_0 + a_1 T^{p/2} + a_2 T^{1/2})} + b'T^2, \tag{1}$$

$$\rho(T) = \frac{1}{\sigma_0 + a_3 \ln T} + b'T^2, \tag{2}$$

where σ_0 is the residual conductivity ($1/\rho_0$), $a_1 T^{p/2}$ accounts for the 3D WL contributions, and $a_2 T^{1/2}$ is attributed to the 3D REEI corrections, and $a_3 \ln T$ is accredited to the combined contributions of the WL and REEI in the 2D limit. The variable p is the index of localization effects in the system and can be influenced by different types of scattering mechanisms. The value of $p = 2$ implies the dominance of electron-electron scattering, whereas $p = 3$ is attributed to electron-phonon scattering [34]. The last term ($b'T^2$) accounts for the Boltzmann term and implies the classical low-temperature dependence of resistivity withholding the Matthiessen rule [71]. We use Eq. (1) to fit the experimental data using a combination of 3D WL and REEI at low temperatures (below 100 K), as shown by the solid lines in Figs. 5(a) and 5(b). Moreover, in Figs. 4(c) and 4(d) of [39] we show a comparison of the residual resistivity, $\Delta\rho(\%) = [\rho_{\text{fit}}(T) - \rho(T)]/\rho(T) \times 100\%$ by fitting the zero-field data considering the WL plus REEI corrections in both 3D (solid red circles) and 2D (solid blue triangles) limits for the $x = 0.025$ and 0.05 samples, respectively. This clearly shows a larger deviation with respect to the zero line in case of the 2D limit as compared to the 3D limit, which confirms the dominance of the 3D limit of WL plus REEI corrections. Now to understand the origin of the quantum effects whether from WL or REEI [34,70], we measure the resistivity of the $x = 0.05$ sample at high applied magnetic fields of 7 and 14 T and present in Fig. 5(b). We find that a higher magnetic field reduces the resistivity and shifts the minimum point slightly towards the low temperatures [as shown in the inset of Fig. 5(b)]. This suggests for diminishing of the QCC effects, which can be attributed to the suppression of wave coherence of the electron under an applied magnetic field and gives a strong evidence

of the WL correction at low temperatures because the REEI correction should be independent of the magnetic field [34]. Further, in Fig. 5(b), we compare the fitting [using Eq. (1)] of resistivity data measured at 0, 7, and 14 T. The obtained values of σ_0 (open red triangles) and a_1 (open blue circles) from the fitting at low temperatures (<100 K) are plotted in Fig. 5(c) on the left and right axes, respectively. A significant increase in σ_0 can be correlated to the negative magnetoresistance and a decrease in the value of a_1 is attributed to the reduction of the quantum corrections with the magnetic field and manifests the dominance of WL effects. The parameters obtained from the low-temperature fit for the $x = 0.025$ and 0.05 samples are summarized in Table III of [39].

In order to analyze the resistivity behavior in the intermediate temperature range (120–200 K), we use the power law to fit the least-square minimization to the experimental data [see Figs. 5(a) and 5(b)]:

$$\rho(T) = \rho_0 + AT^n, \tag{3}$$

where ρ_0 is the residual resistivity, n and A are the fitting parameters to be utilized to quantify the disorder in the FM oxides [34]. In the present case, the ρ_0 values are estimated in the range 8–11×10^{-5} Ω cm for both the samples (see Table III of [39]). The values of coefficient $A = 0.4$–1.5×10^{-11} Ω cm K^{-2} are found to be comparable to the values obtained for the elemental ferromagnets, which are attributed due to electron-electron scattering [72]. Also, in ferromagnetic metal oxides, n values can be used to quantify the disorder; for example, Herranz et al. reported the n value change from ~ 1.1 to 3 for the weak and strong disorder systems, respectively [71]. In our case, the n value is found to be 2.9 ± 0.05 for both samples at zero magnetic field, which suggests the presence of strong disorder in the system. This is also consistent with the observed nonlinearity in ρ-T behavior and the coexistence of FM ordering and metal-insulator transition in these samples [34]. Moreover, the fitting parameters A (open magenta rhombus), ρ_0 (open green triangles), and n (open cyan circles) are plotted on the left and right axes of Fig. 5(d), respectively. The exponent n decreases from 2.95 (0 T) to 2.75 (14 T), which manifests a decrease in the disorder with the applied magnetic field [71]. The fitting parameters obtained using Eq. (2) are included in Table III of [39] for the $x = 0.025$ and 0.05 samples. Further, the analysis of the ρ-T behavior of $x = 0.025$ and 0.05 samples [Figs. 5(a) and 5(b)] in the high-temperature range ($T > T_{\text{MO}}$) is important to study the effect of disorder on the electron-phonon coupling; therefore, we use the electronic transport theory based on Bloch-Grüneisen law, as given below [71,73]:

$$\rho = \rho_0 + \rho_m + \frac{2\pi k_B}{\hbar e^2 (n/m_{\text{eff}})} G(\Theta_D/T) \lambda' T$$
$$= \rho_0 + \rho_m + \gamma(T)T, \tag{4}$$

where ρ_0, ρ_m, and $\gamma(T)$ are the residual resistivity, magnetic resistivity due to the spin scattering of the electrons (considered constant in paramagnetic phase at $T > T_{\text{MO}}$), and $\gamma(T)$ is the temperature-dependent Grüneisen parameter, respectively. Here, $\gamma(T)$ is considered equal to $[2\pi k_B/\hbar e^2 (n/m_{\text{eff}})]G(\Theta_D/T)\lambda'$, where n is the carrier density, m_{eff} is the effective mass of carriers, $G(\Theta_D/T)$ is the
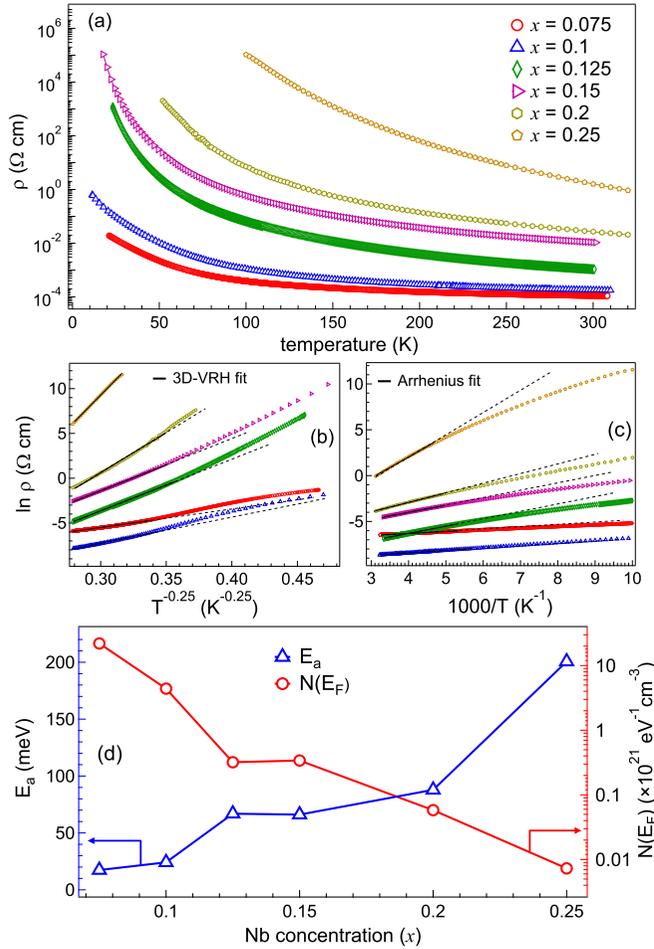
FIG. 6. (a) A comparison of the temperature-dependent resistivity variation of $x = 0.075$–0.25 samples on the semilogarithmic scale, (b) the low-temperature resistivity fitted with the 3D VRH model, and (c) the high-temperature resistivity data fitted with the Arrhenius model; a solid black line presents the fit for the corresponding model and the dotted lines mark the range where the experimental curve deviates from the respective fits, and (d) the activation energy (E_a) extracted from the Arrhenius model on a linear scale and density of states near the Fermi level [$N(E_F)$] extracted from the 3D VRH model on a semilogarithmic scale.

Grüneisen function. The values of $\gamma(T)$ are determined from the slope of the temperature-dependent linear fit of $\rho(T)$ in the high-temperature range [71] [see Figs. 5(a) and 5(b)]. The obtained fitting parameters are presented in Table III of [39], where the $\gamma(T)$ values are found to be 31×10^{-8} Ω cm K^{-1} for the $x = 0.025$, which is much higher as compared to the $x = 0.05$ sample 6×10^{-8} Ω cm K^{-1}. This manifests a higher degree of disorder in the $x = 0.025$ sample. Further, for the $x = 0.05$ sample, there is no significant change in the values of fitting parameters [ρ_0, ρ_m, and $\gamma(T)$] with the applied magnetic field, which suggests invariance of disorder at high temperatures.

In Fig. 6(a), we present the temperature-dependent resistivity data (on a semilogarithmic scale) of the $0.075 \leqslant x \leqslant 0.25$ samples, which clearly show an increasing trend with decreasing temperature, i.e., a semiconducting/insulating na-

ture. Interestingly, the resistivity increases monotonously with x due to higher Nb^{5+} concentration, which predominantly favors the insulating nature of these samples. This observation further confirms that the substitution of Nb^{5+} converts metallic Co^{4+} ions into Co^{3+}, which restricts the metallic conduction pathways. Moreover, the Nb^{5+} does not participate in conduction due to the unavailability of conduction electrons in $4d^0$. In order to understand the possibility of carrier conduction mechanisms in these samples, we analyze the experimental data in two different regions, the high-temperature (320–200 K) with the Arrhenius model (where charge carriers move through the band conduction) and the low-temperature region (160–60 K) with the three-dimensional variable range hopping (3D-VRH) model (where charge carriers move between the ions through nearest-neighbor hopping in the delocalized states). The Arrhenius model can be expressed as [6] $\rho(T) = \rho_0 \exp(E_a/k_B T)$, where ρ_0 and E_a are the exponential prefactor and activation energy, respectively. In Fig. 6(c), we show the $\ln(\rho)$ with 1000/T, and the slope of linear fit (solid black line) of these curves is utilized to determine the activation energy for each sample. The obtained values of activation energy are presented on the left axis of Fig. 6(d) in a linear scale, where we obtain a monotonous enhancement of the activation energy, which is consistent with the dominance of insulating nature with x. Interestingly, a deviation of the experimental data from the Arrhenius model towards low temperatures (highlighted with the dotted black line) demonstrates a possibility of a different conduction mechanism [50]. Therefore, we follow the three-dimensional variable-range hopping (3D VRH) model, which can be given as [6] $\rho(T) = \rho_0 \exp(\frac{T_0}{T})^{1/4}$, where ρ_0 and T_0 are the exponential factors and characteristic temperatures, respectively. In Fig. 6(b), the best fit of the plot between $\ln(\rho)$ and $T^{-1/4}$ validates the 3D VRH model in the low-temperature range, and the dotted black lines are shown where a deviation in the experimental data from the 3D VRH model is visible. The slope of the linear fit is used to determine the characteristic temperature (T_0) and that is used to calculate the density of states (DOS) near the Fermi level [$N(E_F)$] using the formula $N(E_F) = 18/k_B T_0 \lambda^3$, where λ is the localization length of the conduction path. Moreover, the conducting path for the VRH is chosen here (Co/Nb)–O–(Co/Nb) and its value is determined from the Rietveld refinement for the calculation of the DOS. We show the variation in DOS on the right axis of Fig. 6(d) in a semilogarithmic scale, which manifests a monotonous decrease in $N(E_F)$ with x. Further, for the confirmation of the VRH model, we estimate the values of mean hopping distance (R_H) and means hopping energy (W_H), as given below [74]:

$$R_H = [9\lambda/8\pi kTN(E_F)]^{1/4} \text{ nm}, \qquad (5)$$

$$W_H = [3/4\pi R_H^3 N(E_F)] \text{ eV}. \qquad (6)$$

The calculated values of R_H and W_H are found to increase with x, as presented in Table III of [39]. The obtained parameters for the $x \geqslant 0.075$ samples fulfill Mott's criteria for VRH conduction, $\lambda^{-1}R_H \gg 1$ and $W_H \gg k_B T$, at low temperatures below 160 K. These results manifest the magnetic dilution due to Nb^{5+} ($4d^0$) substitution, which leads to the reduction in the conduction pathways for the electron hopping and drives the system toward a more insulating state. We also note here that
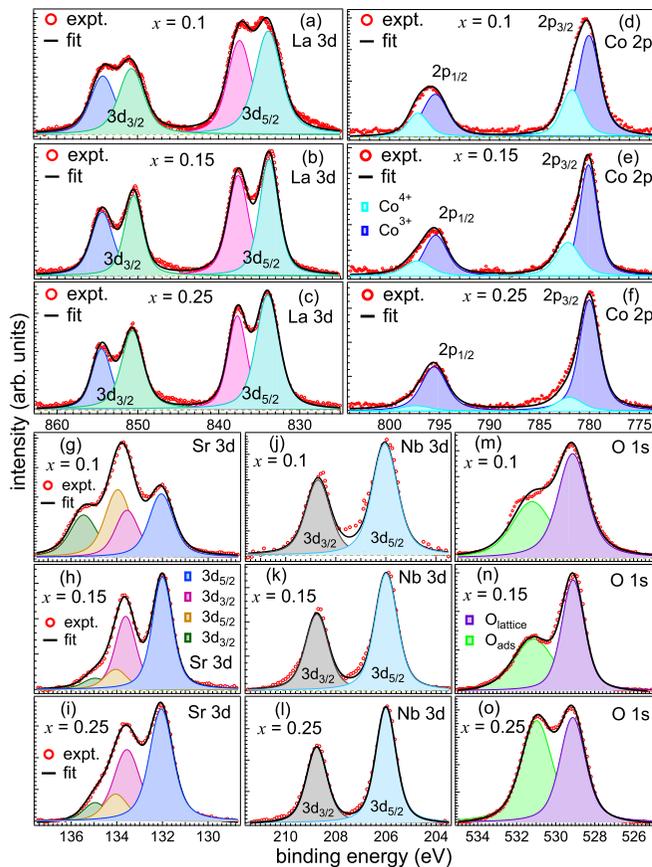
FIG. 7. The core-level x-ray photoemission spectra measured at room temperature and the deconvoluted components of (a)–(c) La $3d$, (d)–(f) Co $2p$, (g)–(i) Sr $3d$, (j)–(l) Nb $3d$, and (m)–(o) O $1s$ for the $x = 0.1$, 0.15, and 0.25 samples.

the temperature-dependent resistivity analysis includes the effect of the scattering of charge carriers at the grain boundary due to the polycrystalline nature of these samples [75,76].

Finally, we investigate the electronic properties of the $x = 0.1$, 0.15, and 0.25 samples using core-level photoemission spectroscopy. In Figs. 7(a)–7(c), we present the core-level La $3d$ spectra, which show two peaks in each spin-orbit component of $3d_{5/2}$ and $3d_{3/2}$ having a separation ≈ 3.8 eV due to the transfer of the electron to the La $4f^0$ from the oxygen valence band [16,77]. Here, the binding energy (BE) values for the main components are 850.6 eV ($3d_{3/2}$) and 833.8 eV ($3d_{5/2}$) having a separation of 16.8 eV confirm the presence of La^{3+} ions [16,77]. More importantly, the spin-orbit split components $2p_{3/2}$ and $2p_{1/2}$ of Co $2p$ core levels are shown in Figs. 7(d)–7(f). The deconvolution of Co $2p_{3/2}$ with two peaks corresponds to the 3+ and 4+ oxidation states, where the BE of Co^{3+} ions is 780 eV ($2p_{3/2}$) and 795.5 eV ($2p_{1/2}$), wheres the Co^{4+} is found to be at 782.0 eV ($2p_{3/2}$) and 797.4 eV ($2p_{1/2}$), both having a separation of ≈ 15.5 eV, which are in good agreement with Refs. [78,79]. There is no signature of any satellite feature at 6 eV from the main peak of Co $2p$ core levels, which confirms the absence of Co^{2+} [79] in the $x = 0.1$, 0.15, and 0.25 samples [see in Figs. 7(d)–7(f)]. These results also conclude that the substitution of Nb^{5+} converts Co^{4+} ions into Co^{3+} ions [13,80]. Further, we determine the average valence (n) of the Co ions

from the area ratio of the deconvoluted components and found it 68% (Co^{3+}) and 32% (Co^{4+}) for the $x = 0.1$ sample, and 72% (Co^{3+}) and 28% (Co^{4+}) for the $x = 0.15$ sample, which manifests an average valence of 3.32 ($x = 0.1$) and 3.28 ($x = 0.15$), and are found to be in good agreement with theoretically determined values of 3.34 and 3.24, respectively. For the $x = 0.25$ sample, the ratio is 88% (Co^{3+}) and 12% (Co^{4+}) having an average valence of 3.1, which is slightly higher than the theoretically calculated value of 3. Further, in Figs. 7(g)–7(i) we present the Sr $3d$ core levels, which are deconvoluted with four components. The two strong components at the lower BE side are observed at 132 eV ($3d_{5/2}$) and 133.6 eV ($3d_{3/2}$) with a separation of 1.6 eV, which are in good agreement with the values reported for the Sr^{2+} valence state [78,81]. The other two weaker components at around 134.0 eV ($3d_{5/2}$) and 135.3 ($3d_{3/2}$) are from SrCO$_3$ traces present on the surface of the sample [81]. Moreover, the Nb $3d$ core levels are presented in Figs. 7(j)–7(l) for the $x = 0.1$, 0.15, and 0.25 samples, respectively, where the deconvoluted components at 206 eV ($3d_{5/2}$) and 208.8 eV ($3d_{3/2}$) with 2.8-eV separation. These values are in good agreement with Refs. [6,78] and confirm the 5+ oxidation state of Nb in these samples. The O $1s$ core-level spectra in Figs. 7(m)–7(o) are deconvoluted into two peaks at the BE values of 529 and 531.1 eV, which correspond to the contributions from the lattice oxygen and surface adsorbed oxygen, respectively [82].

IV. CONCLUSIONS

In conclusion, we have investigated the evolution of structural, magnetic, and transport properties of bulk La$_{0.5}$Sr$_{0.5}$Co$_{1-x}$Nb$_x$O$_3$ ($x = 0.025$–0.25). The Rietveld refinement of the x-ray diffraction patterns with $R\bar{3}c$ space group reveals that the lattice parameters and rhombohedral distortion monotonously increase with the increased Nb concentration. The magnetic susceptibility data manifest that the Nb substitution dilutes the double-exchange interaction and a decrease in the magnetic ordering temperature and net magnetization are observed with x. Interestingly, for the $x > 0.1$ samples, the magnetic interactions are dominated by the superexchange antiferromagnetic interactions. Moreover, the isothermal MH loops recorded at 5 K for the $x > 0.1$ samples manifest that coercivity (H_C) and remanence (M_r) decrease with x due to the dominance of AFM interactions and reduction of FM volume fractions. More interestingly, we observe a minimum in resistivity for the $x = 0.025$ and 0.05 samples, which are analyzed using the quantum corrections in the conductivity where the weak localization effect dominates over the renormalized electron-electron interactions in the 3D limit. Moreover, a semiconducting behavior is observed for the $x > 0.05$ samples, and the resistivity monotonously increases with higher Nb^{5+}($4d^0$) concentration. This semiconducting resistivity behavior is analyzed with the Arrhenius model in the high-temperature (~ 160–320 K) and 3D variable range hopping conduction in the low-temperature region (< 160 K). Further, the core-level photoemission spectra of La $3d$, Sr $3d$, Co $2p$, Nb $3d$, and O $1s$ confirm the valence state of constituent elements and affirm the absence of Co^{2+}, which are in accordance with the magnetization results.

[1] P. M. Raccah and J. B. Goodenough, First-order localized-electron ⇌ collective-electron transition in LaCoO$_3$, Phys. Rev. **155**, 932 (1967).

[2] S. R. Barman and D. D. Sarma, Photoelectron-spectroscopy investigation of the spin-state transition in LaCoO$_3$, Phys. Rev. B **49**, 13979 (1994).

[3] M. Abbate, J. C. Fuggle, A. Fujimori, L. H. Tjeng, C. T. Chen, R. Potze, G. A. Sawatzky, H. Eisaki, and S. Uchida, Electronic structure and spin-state transition of LaCoO$_3$, Phys. Rev. B **47**, 16124 (1993).

[4] C. Zobel, M. Kriener, D. Bruns, J. Baier, M. Grüninger, T. Lorenz, P. Reutler, and A. Revcolevschi, Evidence for a low-spin to intermediate-spin state transition in LaCoO$_3$, Phys. Rev. B **66**, 020402(R) (2002).

[5] A. Chainani, M. Mathew, and D. D. Sarma, Electron-spectroscopy study of the semiconductor-metal transition in La$_{1-x}$Sr$_x$CoO$_3$, Phys. Rev. B **46**, 9976 (1992).

[6] R. Shukla and R. S. Dhaka, Anomalous magnetic and spin glass behavior in Nb-substituted LaCo$_{1-x}$Nb$_x$O$_3$, Phys. Rev. B **97**, 024430 (2018).

[7] M. A. Señarís-Rodríguez and J. B. Goodenough, LaCoO$_3$ Revisited, J. Solid State Chem. **116**, 224 (1995).

[8] K. Asai, O. Yokokura, N. Nishimori, H. Chou, J. M. Tranquada, G. Shirane, S. Higuchi, Y. Okajima, and K. Kohn, Neutron-scattering study of the spin-state transition and magnetic correlations in La$_{1-x}$Sr$_x$CoO$_3$ ($x = 0$ and 0.08), Phys. Rev. B **50**, 3025 (1994).

[9] M. W. Haverkort, Z. Hu, J. C. Cezar, T. Burnus, H. Hartmann, M. Reuther, C. Zobel, T. Lorenz, A. Tanaka, N. B. Brookes, H. H. Hsieh, H.-J. Lin, C. T. Chen, and L. H. Tjeng, Spin State Transition in LaCoO$_3$ Studied Using Soft X-ray Absorption Spectroscopy and Magnetic Circular Dichroism, Phys. Rev. Lett. **97**, 176405 (2006).

[10] A. Podlesnyak, S. Streule, J. Mesot, M. Medarde, E. Pomjakushina, K. Conder, A. Tanaka, M. W. Haverkort, and D. I. Khomskii, Spin-State Transition in LaCoO$_3$: Direct Neutron Spectroscopic Evidence of Excited Magnetic States, Phys. Rev. Lett. **97**, 247208 (2006).

[11] M. A. Korotin, S. Yu. Ezhov, I. V. Solovyev, V. I. Anisimov, D. I. Khomskii, and G. A. Sawatzky, Intermediate-spin state and properties of LaCoO$_3$, Phys. Rev. B **54**, 5309 (1996).

[12] S. Yamaguchi, Y. Okimoto, and Y. Tokura, Local lattice distortion during the spin-state transition in LaCoO$_3$, Phys. Rev. B **55**, R8666(R) (1997).

[13] R. Shukla, A. Jain, M. Miryala, M. Murakami, K. Ueno, S. M. Yusuf, and R. S. Dhaka, Spin dynamics and unconventional magnetism in insulating La$_{(1-2x)}$Sr$_{2x}$Co$_{(1-x)}$Nb$_x$O$_3$, J. Phys. Chem. C **123**, 22457 (2019).

[14] G. Vankó, J.-P. Rueff, A. Mattila, Z. Németh, and A. Shukla, Temperature- and pressure-induced spin-state transitions in LaCoO$_3$, Phys. Rev. B **73**, 024424 (2006).

[15] K. Sato, A. Matsuo, K. Kindo, Y. Kobayashi, and K. Asai, Field-induced spin-state transition in LaCoO$_3$, J. Phys. Soc. Jpn. **78**, 093702 (2009).

[16] R. Prakash, R. Shukla, P. Nehla, A. Dhaka, and R. S. Dhaka, Tuning ferromagnetism and spin state in La$_{1-x}$A$_x$CoO$_3$ (A = Sr, Ca) nanoparticles, J. Alloys Compd. **764**, 379 (2018).

[17] M. A. Señarís-Rodríguez and J. B. Goodenough, Magnetic and Transport Properties of the System La$_{1-x}$Sr$_x$CoO$_{3-\delta}$ ($0 < x \leqslant$ 0.50), J. Solid State Chem. **118**, 323 (1995).

[18] K. Muta, Y. Kobayashi, and K. Asai, Magnetic, Electronic transport, and calorimetric investigations of La$_{1-x}$Ca$_x$CoO$_3$ in comparison with La$_{1-x}$Sr$_x$CoO$_3$, J. Phys. Soc. Jpn. **71**, 2784 (2002).

[19] J. A. Dias, M. A. S. Andrade Jr, H. L. S. Santos, M. R. Morelli, and L. H. Mascaro, Lanthanum-based perovskites for catalytic oxygen evolution reaction, ChemElectroChem **7**, 3173 (2020).

[20] K. Huang, H. Y. Lee, and J. B. Goodenough, Sr and Ni-doped LaCoO$_3$ and LaFeO$_3$ perovskites: New cathode materials for solid-oxide fuel cells, J. Electrochem. Soc. **145**, 3220 (1998).

[21] E. Muhumuza, P. Wu, T. Nan, L. Zhao, P. Bai, S. Mintova, and Z. Yan, Perovskite-type LaCoO$_3$ as an efficient and green catalyst for sustainable partial oxidation of cyclohexane, Ind. Eng. Chem. Res. **59**, 21322 (2020).

[22] N. Zhang, E. Liu, H. Chen, J. Hou, C. Li, and H. Wan, High-performance of LaCoO$_3$/Co$_3$O$_4$ nanocrystal as anode for lithium-ion batteries, Colloid. Surf. A: Phys. Eng. **628**, 127265 (2021).

[23] S. G. Chandrappa, P. Moni, D. Chen, G. Karkera, K. R. Prakash, R. A. Caruso, and A. S. Prakash, The influence of ruthenium substitution in LaCoO$_3$ towards bi-functional electrocatalytic activity for rechargeable Zn-air batteries, J. Mater. Chem. A **8**, 20612 (2020).

[24] R. D. Shannon, Revised effective ionic radii and systematic studies of interatomic distances in halides and chalcogenides, Acta Crystallogr., Sect. A **32**, 751 (1976).

[25] M. Imada, A. Fujimori, and Y. Tokura, Metal-insulator transitions, Rev. Mod. Phys. **70**, 1039 (1998).

[26] A. Mineshige, M. Inaba, T. Yao, Z. Ogumi, K. Kikuchi, and M. Kawase, Crystal structure and metal-insulator transition of La$_{1-x}$Sr$_x$CoO$_3$, J. Solid State Chem. **121**, 423 (1996).

[27] M. Itoh, I. Natori, S. Kubota, and K. Motoya, Spin-glass behavior and magnetic phase diagram of La$_{1-x}$Sr$_x$CoO$_3$ ($0 \leqslant x \leqslant 0.5$) studied by magnetization measurements, J. Phys. Soc. Jpn. **63**, 1486 (1994).

[28] J. Wu, J. W. Lynn, C. J. Glinka, J. Burley, H. Zheng, J. F. Mitchell, and C. Leighton, Intergranular Giant Magnetoresistance in a Spontaneously Phase Separated Perovskite Oxide, Phys. Rev. Lett. **94**, 037201 (2005).

[29] N. Khan, P. Mandal, K. Mydeen, and D. Prabhakaran, Magnetoelectronic phase separation in La$_{1-x}$Sr$_x$CoO$_3$ single crystals:

Evidence from critical behavior, Phys. Rev. B **85**, 214419 (2012).

[30] J. Mira, J. Rivas, M. Vázquez, J. M. García-Beneytez, J. Arcas, R. D. Sánchez, and M. A. Señarís-Rodríguez, Critical exponents of the ferromagnetic-paramagnetic phase transition of $La_{1-x}Sr_xCoO_3$ ($0.20 \leqslant x \leqslant 0.30$), Phys. Rev. B **59**, 123 (1999).

[31] D. Phelan, D. Louca, S. Rosenkranz, S.-H. Lee, Y. Qiu, P. J. Chupas, R. Osborn, H. Zheng, J. F. Mitchell, J. R. D. Copley, J. L. Sarrao, and Y. Moritomo, Nanomagnetic Droplets and Implications to Orbital Ordering in $La_{1-x}Sr_xCoO_3$, Phys. Rev. Lett. **96**, 027201 (2006).

[32] C. He, M. A. Torija, J. Wu, J. W. Lynn, H. Zheng, J. F. Mitchell, and C. Leighton, Non-Griffiths-like clustered phase above the Curie temperature of the doped perovskite cobaltite $La_{1-x}Sr_xCoO_3$, Phys. Rev. B **76**, 014401 (2007).

[33] N. B. Ivanova, S. G. Ovchinnikov, M. M. Korshunov, I. M. Eremin, and N. V. Kazak, Specific features of spin, charge, and orbital ordering in cobaltites, Phys.-Usp. **52**, 789 (2009).

[34] P. A. Lee and T. V. Ramakrishnan, Disordered electronic systems, Rev. Mod. Phys. **57**, 287 (1985).

[35] M. Kriener, C. Zobel, A. Reichl, J. Baier, M. Cwik, K. Berggold, H. Kierspel, O. Zabara, A. Freimuth, and T. Lorenz, Structure, magnetization, and resistivity of $La_{1-x}M_xCoO_3$ ($M =$ Ca, Sr, and Ba), Phys. Rev. B **69**, 094417 (2004).

[36] D. Samal and P. S. Anil Kumar, A critical re-examination and a revised phase diagram of $La_{1-x}Sr_xCoO_3$, J. Phys.: Condens. Matter **23**, 016001 (2011).

[37] A. Kumar, B. Schwarz, H. Ehrenberg, and R. S. Dhaka, Evidence of discrete energy states and cluster-glass behavior of $Sr_{2-x}La_xCoNbO_6$, Phys. Rev. B **102**, 184414 (2020).

[38] A. Kumar, R. Shukla, R. Kumar, R. J. Choudhary, S. N. Jha, and R. S. Dhaka, Electronic and local structure investigation of $Sr_{2-x}La_xCoNbO_6$ using near-edge and extended x-ray absorption fine structures, Phys. Rev. B **105**, 245155 (2022).

[39] See Supplemental Material at http://link.aps.org/supplemental/ 10.1103/PhysRevB.107.165108 for further information about the structural parameters obtained from the Rietveld refinement of the x-ray diffraction patterns, results obtained from the magnetization measurements, and fitting of the experimental transport data using different models.

[40] A. Kumar, A. Jain, S. M. Yusuf, and R. S. Dhaka, Observation of anisotropic thermal expansion and Jahn-Teller effect in double perovskites $Sr_{2-x}La_xCoNbO_6$ using neutron diffraction, J. Phys. Chem. Lett. **13**, 3023 (2022).

[41] R. P. Haggerty, and R. Seshadri, Oxygen stoichiometry, crystal structure, and magnetism of $La_{0.5}Sr_{0.5}CoO_{3-\delta}$, J. Phys.: Condens. Matter **16**, 6477 (2004).

[42] G. H. Jonkar and J. H. Van Santen, Magnetic Compounds with Perovskite Structure III. Ferromagnetic Compounds of Cobalt, Physica (Amsterdam) **19**, 120 (1953).

[43] V. G. Bhide, D. S. Rajoria, C. N. R. Rao, G. R. Rao, and V. G. Jadhao, Itinerant-electron ferromagnetism in $La_{1-x}Sr_xCoO_3$: A Mössbauer study, Phys. Rev. B **12**, 2832 (1975).

[44] D. N. H. Nam, K. Jonason, P. Nordblad, N. V. Khiem, and N. X. Phuc, Coexistence of ferromagnetic and glassy behavior in the $La_{0.5}Sr_{0.5}CoO_3$ perovskite compound, Phys. Rev. B **59**, 4189 (1999).

[45] T. A. Ho, P. T. Long, N. V. Quang, S. L. Cho, and S. C. Yu, Short and long-range ordering in $La_{1-x}Sr_xCoO_3$ cobaltites, J. Magn. Magn. Mater. **477**, 396 (2019).

[46] N. V. Khiem, N. X. Phuc, T.-L. Phan, S.-C. Yu, and M.-H. Phan, Spin dynamics and magnetic frustration effects in $La_{1-x}Sr_xCoO_3$ ($0 < x \leqslant 0.5$) compounds, J. Appl. Phys. **97**, 10A509 (2005).

[47] K. Yoshii and H. Abe, Doping effects of Ru in $L_{0.5}Sr_{0.5}CoO_3$ ($L =$ La, Pr, Nd, Sm, and Eu), Phys. Rev. B **67**, 094408 (2003).

[48] S. Mukherjee, P. Raychaudhuri, and A. K. Nigam, Critical behavior in $La_{0.5}Sr_{0.5}CoO_3$, Phys. Rev. B **61**, 8651 (2000).

[49] A. Podlesnyak, G. Ehlers, M. Frontzek, A. S. Sefat, A. Furrer, Th. Strässle, E. Pomjakushina, K. Conder, F. Demmel, and D. I. Khomskii, Effect of carrier doping on the formation and collapse of magnetic polarons in lightly hole-doped $La_{1-x}Sr_xCoO_3$, Phys. Rev. B **83**, 134430 (2011).

[50] A. Kumar and R. S. Dhaka, Unraveling the magnetic interactions and spin state in insulating $Sr_{2-x}La_xCoNbO_6$, Phys. Rev. B **101**, 094434 (2020).

[51] T. Sarkar, V. Pralong, and B. Raveau, Formation of magnetic glass in calcium-doped $YBaCo_2O_{5.5}$ cobaltites, Phys. Rev. B **83**, 214428 (2011).

[52] Z.-H. Wang, X. Chen, B.-G. Shen, Y.-D. Zhang, J.-W. Cai, R.-W. Li, J.-G. Zhao, and W.-S. Zhan, Magnetic glass behavior and magnetoresistive properties of perovskite cobaltites $La_{0.7}Sr_{0.3}Co_{1-y}Ga_yO_3$, Phys. Rev. B **60**, 14541 (1999).

[53] N. Kumar and A. Sundaresan, On the observation of negative magnetization under zero-field-cooled process, Solid State Commun. **150**, 1162 (2010).

[54] Y. Ren, T. T. M. Palstra, D. I. Khomskii, E. Pellegrin, A. A. Nugroho, A. A. Menovsky, and G. A. Sawatzky, Temperature-induced magnetization reversal in a YVO_3 single crystal, Nature (London) **396**, 441 (1998).

[55] B. Sarkar, B. Dalal, and S. K. De, Temperature-induced magnetization reversal in $SrRuO_3$, Appl. Phys. Lett. **103**, 252403 (2013).

[56] L. Ferrari, Chemical and structural disorder effects on the Curie temperature, Philos. Mag. **91**, 3021 (2011).

[57] R. K. Sahu, Effect of Mo doping on magnetic and transport properties of $La_{0.5}Sr_{0.5}CoO_3$, J. Magn. Magn. Mater. **305**, 47 (2006).

[58] P.-G. de Gennes, Effects of double exchange in magnetic crystals, Phys. Rev. **118**, 141 (1960).

[59] J. Du, B. Zhang, R. K. Zheng, and X. X. Zhang, Memory effect and spin-glass-like behavior in Co-Ag granular films, Phys. Rev. B **75**, 014415 (2007).

[60] K. Binder and A. P. Young, Spin glasses: Experimental facts, theoretical concepts, and open questions, Rev. Mod. Phys. **58**, 801 (1986).

[61] S. Mukherjee, R. Ranganathan, P. S. Anil Kumar, and P. A. Joy, Static and dynamic response of cluster glass in $La_{0.5}Sr_{0.5}CoO_3$, Phys. Rev. B **54**, 9267 (1996).

[62] P. A. Joy, P. S. Anil Kumar, and S. K. Date, The relationship between field-cooled and zero-field-cooled susceptibilities of some ordered magnetic systems, J. Phys.: Condens. Matter **10**, 11049 (1998).

[63] X. Xu, L. Jiang, J. Shen, Z. Chen, and Z. Xu, Relationship between the spin state of Co ions and thermopower in $La_{1-x}Sr_xCoO_3$ ($0 \leqslant x \leqslant 0.5$), Phys. Lett. A **351**, 431 (2006).

[64] K. Pandey, R. Basnet, A. Wegner, G. Acharya, M. R. Un Nabi, J. Liu, J. Wang, Y. K. Takahashi, B. Da, and J. Hu, Electronic and magnetic properties of the topological semimetal candidate NdSbTe, Phys. Rev. B **101**, 235161 (2020).

[65] T. Elovaara, H. Huhtinen, S. Majumdar, and P. Paturi, Irreversible metamagnetic transition and magnetic memory in small-bandwidth manganite $Pr_{1-x}Ca_xMnO_3$ ($x = 0.0$-0.5), J. Phys.: Condens. Matter **24**, 216002 (2012).

[66] S. Majumdar, K. Kooser, T. Elovaara, H. Huhtinen, S. Granroth, and P. Paturi, Analysis of electronic structure and its effect on magnetic properties in (001) and (110) oriented $La_{0.7}Sr_{0.3}MnO_3$ thin films, J. Phys.: Condens. Matter **25**, 376003 (2013).

[67] R. Mahendiran and A. K. Raychaudhuri, Magnetoresistance of the spin-state-transition compound $La_{1-x}Sr_xCoO_3$, Phys. Rev. B **54**, 16044 (1996).

[68] A. K. Raychaudhuri, Metal-insulator transition in perovskite oxides: A low-temperature perspective, Adv. Phys. **44**, 21 (1995).

[69] Y. J. Chang, C. H. Kim, S.-H. Phark, Y. S. Kim, J. Yu, and T. W. Noh, Fundamental Thickness Limit of Itinerant Ferromagnetic $SrRuO_3$ Thin Films, Phys. Rev. Lett. **103**, 057201 (2009).

[70] G. Herranz, F. Sánchez, J. Fontcuberta, V. Laukhin, J. Galibert, M. V. García-Cuenca, C. Ferrater, and M. Varela, Magnetic field effect on quantum corrections to the low-temperature conductivity in metallic perovskite oxides, Phys. Rev. B **72**, 014457 (2005).

[71] G. Herranz, V. Laukhin, F. Sánchez, P. Levy, C. Ferrater, M. V. García- Cuenca, M. Varela, and J. Fontcuberta, Effect of disorder on the temperature dependence of the resistivity of $SrRuO_3$, Phys. Rev. B **77**, 165114 (2008).

[72] N. V. Volkenshtein, V. P. Dyakina, and V. E. Startsev, Scattering mechanisms of conduction electrons in transition metals at low temperatures, Phys. Status Solidi B **57**, 9 (1973).

[73] M. Gurvitch, A. K. Ghosh, B. L. Gyorffy, H. Lutz, O. F. Kammerer, J. S. Rosner, and M. Strongin, Effects of Disorder on the Transition Temperature and Transport Properties of a Low-T_c $A15$ Superconductor: Mo_3Ge, Phys. Rev. Lett. **41**, 1616 (1978).

[74] D. K. Paul and S. S. Mitra, Evaluation of Mott's Parameters for Hopping Conduction in Amorphous Ge, Si, and Se-Si, Phys. Rev. Lett. **31**, 1000 (1973).

[75] G. Reiss, J. Vancea, and H. Hoffman, Grain-Boundary Resistance in Polycrystalline Metals, Phys. Rev. Lett. **56**, 2100 (1986).

[76] P. R. Sagdeo, S. Anwar, N. P. Lalla, and S. Patil, The contribution of grain boundary and defects to the resistivity in the ferromagnetic state of polycrystalline manganites, J. Magn. Magn. Mater. **306**, 60 (2006).

[77] D. J. Lam, B. W. Veal, and D. E. Ellis, Electronic structure of lanthanum perovskites with $3d$ transition elements, Phys. Rev. B **22**, 5730 (1980).

[78] A. Kumar, R. Shukla, A. Pandey, S. Dalal, M. Miryala, K. Ueno, M. Murakami, and R. S. Dhaka, Structural, transport, optical, and electronic properties of Sr_2CoNbO_6 thin films, J. Appl. Phys. **128**, 025303 (2020).

[79] T. J. Chuang, C. R. Brundle, and D. W. Rice, Interpretation of the X-ray photoemission spectra of cobalt oxides and cobalt oxide surfaces, Surf. Sci. **59**, 413 (1976).

[80] R. Shukla, A. Kumar, R. Kumar, S. N. Jha, and R. S. Dhaka, X-ray absorption spectroscopy study of $La_{1-y}Sr_yCo_{1-x}Nb_xO_3$, J. Phys. Chem. C **125**, 10130 (2021).

[81] M. I. Sosulnikov and Yu. A. Teterin, X-ray photoelectron studies of Ca, Sr and Ba and their oxides and carbonates, J. Electron Spectrosc. Relat. Phenom. **59**, 111 (1992).

[82] M. Imamura, N. Matsubayashi, and H. Shimada, Catalytically active oxygen species in $La_{1-x}Sr_xCoO_{3-\delta}$ studied by XPS and XAFS spectroscopy, J. Phys. Chem. B **104**, 7348 (2000).